

Deep-Learning-Based Calibration in Contrast Source Inversion Based Microwave Subsurface Imaging

Takahiro Hanabusa, Takahide Morooka, and Shouhei Kidera[✉], *Senior Member, IEEE*

Abstract—A deep-learning (DL)-based data calibration technique applied to quantitative microwave inverse-scattering analysis is presented. This technique aims at subsurface inspection for the buried object under a concrete road or soil. The inverse-scattering analysis provides a complex permittivity profile, which is useful for object identification such as air gap or water. Contrast source inversion (CSI) is one of the most promising inverse-scattering methods. This method is capable of avoiding the iterative use of highly computational forward solvers. However, when applied to the measured data, an appropriate calibration capable of converting measured data to simulation data is required. In this work, a DL-based calibration suitable for nonlinear inverse problems is proposed. Its efficiency is experimentally demonstrated using a concrete cylinder containing water with different salinities.

Index Terms—Contrast source inversion (CSI), deep-learning (DL)-based calibration, inverse scattering analysis, microwave quantitative imaging.

I. INTRODUCTION

EFFICIENT and accurate monitoring tools for massive transportation infrastructure are highly in demand, especially in developed countries, where roads or tunnels are 50 years old or even older. Although nondestructive testing (NDT) techniques, such as the hammering test or ultrasound monitoring, are available, they require a contact measurement to avoid undesired attenuation of the measured signal due to propagation in the air. For large-scale subsurface inspections, these techniques require substantial human effort and time. They also exhibit some difficulties when applied to entire area surveys. These difficulties may lead to overlooking cracks or other aging deterioration. Contrarily, microwave NDT is capable of conducting noncontact subsurface measurements, achieving rapid data acquisition by vehicle-mounted scanning and sufficient penetration depth into a concrete medium.

Many imaging schemes based on subsurface radar qualitative imaging, such as synthetic aperture radar (SAR) [1], have been proposed for microwave NDT monitoring. Although these approaches provide the spatial profile of the reflection

coefficient for buried objects, they cannot retrieve the complex permittivity profile. Also, they face serious problems in recognizing the type of material, such as air, water, saline, or steel pipe. In contrast, the nonlinear inverse-scattering analysis, called the tomography approach, is capable of providing a quantitative profile of the complex permittivity by solving the domain integral equation. Several studies have been performed on linear approximation approaches with regard to subsurface NDT or ground penetrating radar (GPR) observation models [2], [3]. In addition, to alleviate the nonlinear property, many approaches, such as the full-wave inversion [4], the distorted Born iterative method (DBIM) [5], contrast source inversion (CSI) [6], and deep-learning (DL)-enhanced approaches [7], have been proposed. In this letter, we focus on the CSI scheme since it does not require iterative use of a computationally intensive forward solver, if the Green's function of the background media is given as an analytical form, such as the finite-difference time-domain (FDTD) method.

The key point in realizing quantitative imaging using the CSI or other inverse-scattering methods is data calibration, which compensates for the difference between the simulation and real scenarios. Usually, the signal generator, transmitting or receiving antenna, or other fixing jigs, cannot be easily implemented in the simulation model. Therefore, the calibration procedure using some target cases with known dielectric profiles is necessary to produce a complex permittivity profile reconstruction, even when using the CSI scheme. Some calibration procedures, such as the linear transfer function (LTF) scheme [8], [9], have been developed. However, these approaches are incapable of compensating for the nonlinear effects, such as multiple scattering or other multiplicative interference. Fedeli [10] performed a time-domain data conversion from 3-D measurement data to 2-D simulation data via long short-term memory (LSTM). The 1-D convolutional neural network (CNN)-based approach also promises a reduction in the number of trainable parameters. However, the time-series-based approach requires a large number of input dimensions to satisfy the Nyquist criteria and the desired frequency resolutions, thus requiring densely sampled data with sufficient length. Thus, this study focuses on frequency data-based conversion via the deep-neural-network (DNN) process, as a few frequency responses are needed for applying the CSI. While the study in [11] also introduces a frequency data conversion method, it only specifies filtering out of antenna characteristics to be matched with an analytical dipole model and is not oriented to compensate for the other differential factors between simulations and real data.

Manuscript received December 20, 2021; revised March 10, 2022 and April 18, 2022; accepted April 19, 2022. Date of publication April 22, 2022; date of current version May 6, 2022. This work was supported by the Commissioned Research of "National Institute for Land and Infrastructure Management," under the Technology Research and Development System of the Committee on Advanced Road Technology established by Ministry of Land, Infrastructure, Transport and Tourism (MLIT), Japan. (*Corresponding author: Shouhei Kidera.*)

The authors are with the Graduate School of Informatics and Engineering, The University of Electro-Communications, Tokyo 1828585, Japan (e-mail: kidera@uec.ac.jp).

Digital Object Identifier 10.1109/LGRS.2022.3169799

1558-0571 © 2022 IEEE. Personal use is permitted, but republication/redistribution requires IEEE permission.
See <https://www.ieee.org/publications/rights/index.html> for more information.

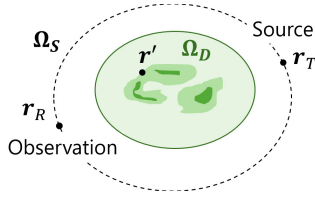


Fig. 1. Observation model.

As a notable feature of the proposed method, the experimental data are effectively converted to corresponding simulation data, including the nonlinear effects, using the 1-D frequency inputs. Thus, less complexity is required in comparison with other higher-dimensional input DNN models. Note that since this study focuses on the DNN-based calibration, it does not require many training datasets, compared with other DNN-based inversion schemes such as in [7], which basically need a sufficient training data to cover various types of dielectric profiles. This is the main advantage of the proposed DNN-based data preprocessing. Experimental tests using a concrete cylinder, which contains different types of objects (e.g., air, pure water, and salinity with different concentrations), demonstrate that the proposed calibration approach is capable of further improving the reconstruction accuracy of scattered data or the dielectric profile obtained using the CSI scheme.

II. CONTRAST SOURCE INVERSION

The 2-D geometry of the observation model, including the observation and object areas, is presented in Fig. 1. Several transmitters and receivers are arranged in the area (defined as Ω_S) surrounding an object. The object existing area is denoted as Ω_D [i.e., the region of interest (ROI)]. All combined data between the transmitters and receivers are used for the reconstruction scheme. $E_{i,j}^T(\mathbf{r})$ and $E_{i,j}^I(\mathbf{r})$ denote the total electric field with and without the object, respectively, where the i th transmitter and receiver are assumed at the j th frequency bin. $E_{i,j}^S(\mathbf{r}) \equiv E_{i,j}^T(\mathbf{r}) - E_{i,j}^I(\mathbf{r})$ is defined as the scattering electric field and is given by the following domain integral as

$$E_{i,j}^S(\mathbf{r}) = k_b^2 \int_{\Omega_D} G_j^b(\mathbf{r}, \mathbf{r}') E_{i,j}^T(\mathbf{r}') \chi_j(\mathbf{r}') d\mathbf{r}' \quad (\mathbf{r} \in \Omega_S) \quad (1)$$

where k_b^2 and $G_j^b(\mathbf{r}, \mathbf{r}')$ denote the wavenumber and Green's function of a background medium, respectively. Ω_S and Ω_D denote the observation domain and ROI, respectively. $\chi_j(\mathbf{r}) \equiv (\epsilon_j(\mathbf{r}) - \epsilon_{b,j}(\mathbf{r}))/\epsilon_{b,j}(\mathbf{r})$ represents the contrast function and $\epsilon_j(\mathbf{r})$ and $\epsilon_{b,j}(\mathbf{r})$ are the complex permittivity of the targets and background media, respectively. The inverse problem, namely, solving $\chi_j(\mathbf{r})$, from the number of scattered fields is nonlinear and ill-posed.

In the CSI method [6], a variable defined as $w_{i,j}(\mathbf{r}) \equiv \chi_j(\mathbf{r}) E_{i,j}^T(\mathbf{r})$ (so-called a contrast source) is originally introduced. In the CSI framework, the total field within the ROI ($\mathbf{r} \in \Omega_D$) can also be expressed as follows:

$$E_{i,j}^T(\mathbf{r}) = E_{i,j}^I(\mathbf{r}) + k_b^2 \int_{\Omega_D} G_j^b(\mathbf{r}, \mathbf{r}') w_{i,j}(\mathbf{r}') d\mathbf{r}' \quad (\mathbf{r} \in \Omega_D). \quad (2)$$

The total field $E_{i,j}^T(\mathbf{r})$, object function $\chi_j(\mathbf{r})$, and contrast source $w_{i,j}(\mathbf{r})$, defined in the ROI, are sequentially optimized using the cost function, which satisfies both (1) and (2), detailed in [6].

III. CALIBRATION METHOD

A quantitative profile of an object's complex permittivity can be obtained by employing an appropriate calibration procedure to convert the experimental data into numerical data, such as FDTD data. Once the experimental data are converted, all post-processing in the CSI can be performed numerically. Note that in the CSI scheme, $E_{j,k}^T(\mathbf{r})$ and $E_{j,k}^I(\mathbf{r})$ ($\mathbf{r} \in \Omega_S$) in (1) are required. However, these components are affected by the actual antenna characteristics, mutual couplings, the propagation loss in the RF cable, or other clutter components, which are difficult to be considered in the analytical form or numerical computation. Thus, an appropriate calibration strategy is required. Next, the two calibration methods are introduced as follows.

A. LTF-Based Calibration

The experimental data are converted into numerical data by first introducing the LTF model, which has been proposed in [8]. Let $\bar{E}_{i,j}^{T,sim}$ and $\bar{E}_{i,j}^{I,sim}$ be the total and incident electric fields, respectively, generated by the FDTD method, assuming a calibration object with a known complex permittivity profile at the i th transmitter and receiver pair of the j th frequency point. In addition, $\bar{S}_{i,j}^{T,exp}$ and $\bar{S}_{i,j}^{I,exp}$ be the S_{21} parameter in the experiment with and without calibration objects buried in concrete background media, respectively. $\bar{E}_{i,j}^{S,sim} \equiv \bar{E}_{i,j}^{T,sim} - \bar{E}_{i,j}^{I,sim}$ and $\bar{S}_{i,j}^{S,exp} \equiv \bar{S}_{i,j}^{T,exp} - \bar{S}_{i,j}^{I,exp}$ are defined. A compensation coefficient $\zeta_{i,j}$ is introduced as follows:

$$\zeta_{i,j} \equiv \frac{\bar{E}_{i,j}^{T,sim} - \bar{E}_{i,j}^{I,sim}}{\bar{S}_{i,j}^{T,exp} - \bar{S}_{i,j}^{I,exp}}. \quad (3)$$

Let $S_{i,j}^{S,exp}$ be the scattered field produced by an unknown object. This is converted to the corresponding simulation data as $\tilde{E}_{i,j}^{S,sim} = \zeta_{i,j} S_{i,j}^{S,exp}$. Although this conversion scheme is quite simple and can be applied to a wide range of objects, nonlinear effects, such as multiple scattering or multiplicative interference between clutters, may not be compensated.

B. DNN-Based Calibration

To address the above-mentioned issue, a DNN-based calibration scheme is proposed in this work. Note that the measurement data structure is not in a multidimensional form, but can be well expressed by a 1-D vector of the combination of the frequencies and sensor locations. Thus, in this scenario, 1-D input conversion is performed and a deep multilayer perceptron (MLP) model [12] is introduced. The fully connected MLP model with three hidden layers is shown in Fig. 2.

1) *Training Step*: To only extract the differential feature between the simulation and experimental data, the same observation model with different dielectric profiles corresponding to each calibration target is preliminarily calculated using the FDTD. Thus, the proposed DNN approach could only compensate for the different factors between simulation and

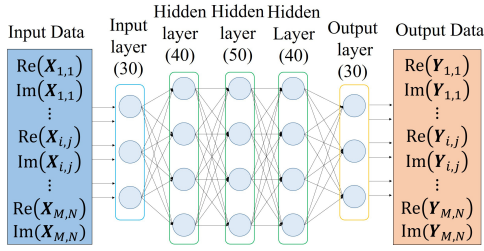


Fig. 2. MLP neural network model.

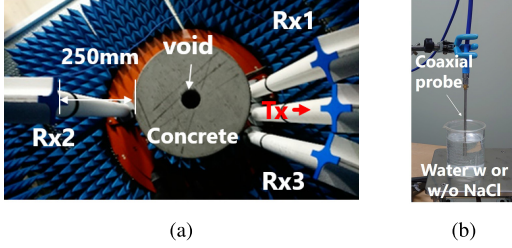


Fig. 3. (a) Experimental setup. (b) Complex permittivity measurement setup using coaxial probe.

real data, which are impervious to dielectric profile variance. In the training process, assuming the calibration scenario described above, the experimental data at each sensor and frequency are converted into simulation data by introducing an input vector \bar{X} , which is defined as $\bar{X} \equiv [\bar{S}_{1,1}^{S,\text{exp}}, \dots, \bar{S}_{1,M}^{S,\text{exp}}, \bar{S}_{2,1}^{S,\text{exp}}, \dots, \bar{S}_{N,M}^{S,\text{exp}}]$, where N and M denote the number of sensors and frequencies, respectively. Additionally, in the training phase, the output vector \bar{Y} is defined as $\bar{Y} \equiv [\bar{E}_{1,1}^{S,\text{sim}}, \dots, \bar{E}_{1,M}^{S,\text{sim}}, \bar{E}_{2,1}^{S,\text{sim}}, \dots, \bar{E}_{N,M}^{S,\text{sim}}]$, where $\bar{E}_{i,j}^{S,\text{sim}}$ represents the scattered data obtained for the same model assumed in the experiment and corresponds to $\bar{S}_{i,j}^{S,\text{exp}}$. In this case, the activation function is the sigmoid function, and the Levenberg–Marquardt algorithm is adopted to minimize the loss function. Although this model is similar to the auto-encoder model, the input and output vectors are not the same. The experimental data are converted into simulation data, considering the nonlinear effect in data calibration.

2) *Data Conversion Step*: After the training process is completed, the scattered field $S_{i,j}^{S,\text{exp}}$ measured at the unknown object is converted using the following input vectors as $X \equiv [S_{1,1}^{S,\text{exp}}, \dots, S_{1,M}^{S,\text{exp}}, S_{2,1}^{S,\text{exp}}, \dots, S_{N,M}^{S,\text{exp}}]$. The virtual simulation data are obtained from the output vectors Y .

IV. RESULTS AND DISCUSSIONS

The experimental setup, considering an NDT model, where a cylindrical concrete material with a 298-mm radius includes a void cylinder with a 50-mm radius, is shown in Fig. 3. The four-dipole antennas along the vertical axis (z -axis) are arranged on the circular circumference, where one transmitter and three receivers are fixed. Rx1 and Rx3 are located at an angle of 20° between the center of the stand and the antennas, namely each separation is 140 mm, and Rx2 faces Tx across the concrete object. These antennas are rotated around the z -axis with an angle step of 5° in the range 0° – 360° , and the scattered data are obtained. $N = 72$ data

TABLE I
TARGET CASE IN THE EXPERIMENT

Case %	
0	No concrete or object
BG	Concrete w/o object
AIR	Concrete w object (Air)
W	Concrete w object (water w/o NaCL)
S-1	Concrete w object (water w NaCL, 4.8 %)
S-2	Concrete w object (water w NaCL, 9.1 %)
S-3	Concrete w object (water w NaCL, 13.0 %)
S-4	Concrete w object (water w NaCL, 16.7 %)
S-5	Concrete w object (water w NaCL, 20.0 %)
S-6	Concrete w object (water w NaCL, 25.5 %)

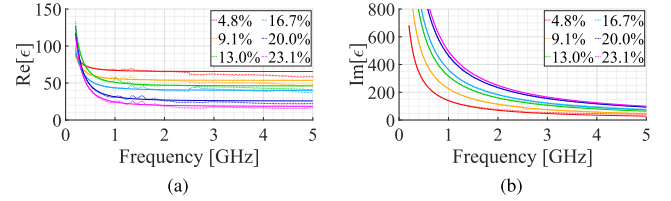


Fig. 4. Frequency dependency of measured complex permittivity (broken line) and Debye fitting curve (solid line) for water with different salinities. (a) Real part of permittivity. (b) Imaginary part of permittivity.

samples were obtained in total. Although the above array arrangement does not match the real NDT or GPR model, it enables the quantitative and reliable assessment of each method. In addition, each received signal includes a strong reflection from the concrete surface and a considerably weaker response from a buried object. These features fairly simulate the measurable data in a real NDT model. The S_{21} scattering parameter at each angle step is recorded using a vector network analyzer, where the frequency is swept from 0.01 to 5.51 GHz with a 10-MHz step, that is, 550 frequency samples. The center void of the cylinder contains different types of liquids, including NaCl, which are summarized in Table I. Fig. 4 shows the frequency dependence of the complex permittivity for objects with different salinities, where the measured S_{11} values can be obtained from the coaxial probe shown in Fig. 3(b) and the Debye fitting curves. It can be observed that the real and imaginary parts of the complex permittivity largely depend on the density of liquid salinity and frequency. In both calibration cases, $M = 15$ different frequency responses ranging from 1.44 to 2.53 GHz were obtained. In the simulation, the 2-D FDTD solver with 2-mm cell size and perfect matching layer (PML) is used, where a point source and receiver are located in the same geometry in the experiment as in Fig. 3. The Gaussian modulated pulse with 2.5-GHz frequency and 2.0-GHz bandwidth is transmitted as the source current in the FDTD. In the training step of the DNN-based method, the cases of “0,” “BG,” “AIR,” “W,” “S-1,” and “S-6” are inputs used as training data. The other cases are used as the test datasets. The number of layers and neurons used are as shown in Fig. 2. The ratios for training, validation, and test data are 70%, 15%, and 15%, respectively. The minimization algorithm for the MLP cost function is Levenberg–Marquardt.

The scatter plots in the different object cases using the LTF model and DNN-based calibration approaches are shown in Fig. 5. In the DNN scheme, the optimal training results are applied in considering both training and validation

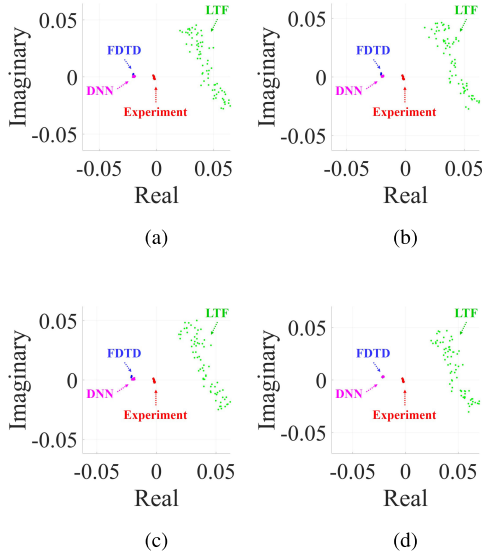


Fig. 5. Scattered plots on the Gaussian plane at 1.43 GHz on the receiver Rx3, using the LTF and DNN calibrations. Red and blue dots denote the experimental and simulation data, respectively. Green and magenta dots denote the converted experimental data, using the LTF and DNN, respectively. (a) S-2. (b) S-3. (c) S-4. (d) S-5.

TABLE II
NRMSES FOR CALIBRATION RESULTS AT 1.43 GHz

Case	w/o calibration	LTF	DNN
S-2	0.90	3.39	0.09
S-3	0.91	3.23	0.12
S-4	0.91	3.17	0.12
S-5	0.90	3.41	0.03

DL curves to avoid the over-fitting problem. Here, the LTF uses the datasets for BG (concrete without object) and AIR (concrete with air) to calculate both $E_{i,j}^{S,sim}$ and $S_{i,j}^{S,exp}$ in (3). The LTF model could not compensate for the difference between the simulation and experimental data, because if the value of $\bar{E}_{i,j}^{S,sim}$ is small in a specific frequency bin, the noise component of the $\bar{S}_{i,j}^{S,exp}$ would be emphasized in (3); this is similar to an inverse filter response. In contrast, the DNN-based method achieved the correct conversion in each case. While the training dataset is relatively small, the proposed scheme could offer sufficient accuracy. Since the DNN scheme could only extract a differential feature between the simulation and experimental data, it does not necessarily require a large amount of training data, unlike other DNN-based inversion approaches. Notably, the processing time for the DNN training process is 1600 s when using a 2.2-GHz Intel Xeon Silver 4210 CPU with 128-GB RAM. As a quantitative analysis, the normalized root mean square errors (NRMSEs) are introduced as $NRMSE = (\sum_{i=1}^N |E_{i,j}^{S,true} - E_{i,j}^{S,est}|^2)^{1/2} / (\sum_{i=1}^N |E_{i,j}^{S,true}|^2)^{1/2}$ where $E_{i,j}^{S,true}$ and $E_{i,j}^{S,est}$ denote the reference and the estimated scattered data at the i th observation sample and the j th frequency sample. N denotes the number of sensors samples (72 in this case). Table II summarizes the NRMSEs for each calibration method at 1.43 GHz, and it clearly demonstrated that the DNN approach accurately converts the

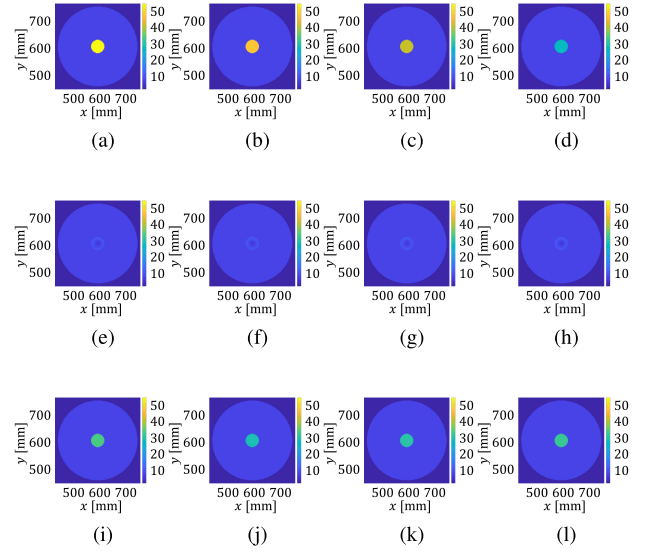


Fig. 6. Reconstruction results for real part of complex permittivity. First line: original. Second line: using LTF calibration. Third line: using DNN calibration. (a), (e), and (i) S-2. (b), (f), and (j) S-3. (c), (g), and (k) S-4. (d), (h), and (l) S-5.

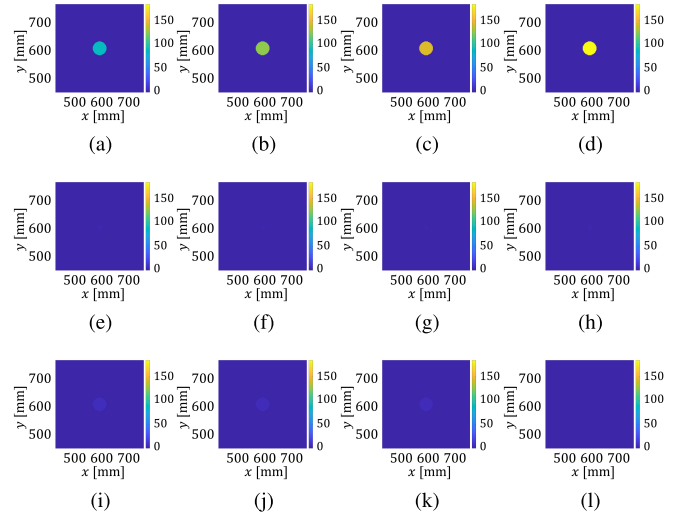


Fig. 7. Reconstruction results for imaginary part of complex permittivity. Each line denotes the same as in Fig. 6. (a), (e), and (i) S-2. (b), (f), and (j) S-3. (c), (g), and (k) S-4. (d), (h), and (l) S-5.

experimental data to the simulation data. Notably, we confirmed that the DNN calibration also provides accurate results at other frequencies. The reconstruction results for the real and imaginary parts of the complex permittivity profiles using the CSI scheme for each test case are shown in Figs. 6 and 7. Here, the multiplicative regularized (MR)-CSI algorithm [13] is introduced, where the maximum iteration number is fixed to 5000, and 15 frequency samples are used. The cell size of the inversion is also 2 mm and the initial estimate of the contrast function is given by the back-projection algorithm [6]. The ROI is considered the original location of the object. It is also demonstrated that the proposed DNN-based conversion provides better reconstruction performance than that obtained using the traditional LTF model. Reconstruction errors are still observed even using the DNN-based calibration. This is due

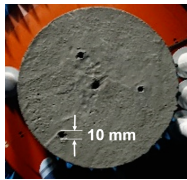


Fig. 8. Experimental objects including four air cavities.

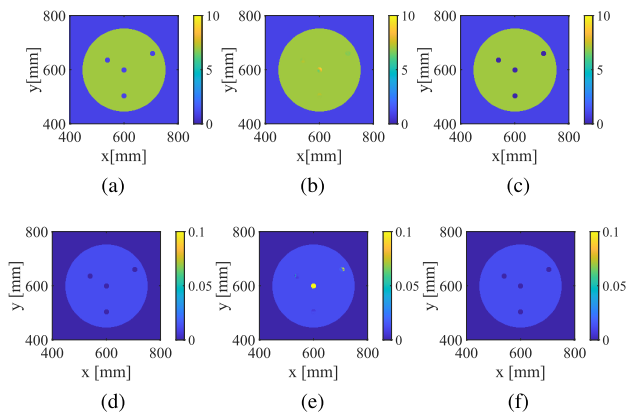


Fig. 9. Reconstruction results of complex permittivity for objects including four air cavities. (a)–(c) $\Re[\epsilon]$. (d)–(f) $\Im[\epsilon]$.

to the complex permittivity inconsistency of concrete media or clutter components such as interactive scattering between an object and its supporting material. Here, the $\Im[\epsilon]$ value is large (>80) even in the *S*-2 case, namely, an incident wave cannot sufficiently penetrate an object region, and the scattered data recorded at Rx2 mainly include creeping waves along the object surface. Notably, the reconstruction results of $\Im[\epsilon]$ are considerably lower than the actual values. This is because the initial value of $\Im[\epsilon]$ is set to zero in the CSI and the solution then could fall into a local minimum.

To validate the applicability of the proposed method, another object case with a different location is investigated as follows. The four air cavities with 10-mm diameters are buried into a concrete cylinder. Note that the same observation model (the number of antennas and the dimension of the concrete cylinder) and the calibration data, that is, the training dataset, assumed in Figs. 6 and 7, are used in this case. Fig. 8 shows the concrete object with four small cavities. Fig. 9 shows the optical image and reconstruction results of the object for real and imaginary parts of the complex permittivity obtained from the LTF and DNN calibration schemes, where the parameters of the CSI, such as iteration number or frequency points, are used. Although the results obtained by the LTF scheme cannot provide a significant profile, the DNN-based approach can provide a dielectric profile at a certain level of accuracy.

V. CONCLUSION

A DNN-based calibration strategy and the corresponding results were presented for the microwave quantitative NDT monitoring scheme. The CSI was introduced as a low-complexity and high-practicability method in the experimental measurement procedure. The experimental results obtained from four different salinity liquid objects buried in a concrete medium demonstrated that the proposed calibration approach is capable of further enhancing the conversion accuracy between the experimental and FDTD-based simulation

data compared with the traditional LTF model. We also confirmed that even if we switch the training and test dataset, the proposed calibration works well, because the proposed scheme in this study simply focuses on the conversion from experimental data to simulation one. Namely, if the same measurement setup is used, it is basically applicable to various dielectric profiles or object sizes. Typically, the calibration accuracies of both the LTF and DNN methods are sensitive to antenna displacement and other observation factors. However, this sensitivity is also an inherent limitation of general calibration techniques. In most calibration approaches, the calibration data should be sequentially rerecorded, after introducing a different observation model, such as an array arrangement, transmitter, or antenna design. Although, when applied to an actual NDT or GPR observation model requiring recalibration data, the proposed scheme uses only a few objects such as homogeneous single-layer materials with known dielectric properties and thicknesses. We plan to apply this method to an actual road model with an available radar module. However, one critical factor, for extending an actual model, is the object size, as our method requires FDTD simulation data assuming the same observation model. In addition, the computational cost would be a bottleneck in dealing with the large investigation area assumed in the NDT or GPR models, and this will be addressed in our future study.

REFERENCES

- [1] M. Fallahpour, J. T. Case, M. Ghasr, and R. Zoughi, "Piecewise and Wiener filter-based SAR techniques for monostatic microwave imaging of layered structures," *IEEE Trans. Antennas Propag.*, vol. 62, no. 1, pp. 1–13, Jan. 2014.
- [2] M. Hajebi and A. Hoorfar, "A multiscale optimization technique for large-scale subsurface profiling," *IEEE Geosci. Remote Sens. Lett.*, vol. 18, no. 10, pp. 1706–1710, Oct. 2021.
- [3] S. Sun, B. J. Kooij, and A. G. Yarovoy, "Linearized 3-D electromagnetic contrast source inversion and its applications to half-space configurations," *IEEE Trans. Geosci. Remote Sens.*, vol. 55, no. 6, pp. 3475–3487, Jun. 2017.
- [4] D. Feng, X. Wang, and B. Zhang, "A frequency-domain quasi-newton-based biparameter synchronous imaging scheme for ground-penetrating radar with applications in full waveform inversion," *IEEE Trans. Geosci. Remote Sens.*, vol. 59, no. 3, pp. 1949–1966, Mar. 2021.
- [5] D. W. Winters, B. D. Van Veen, and S. C. Hagness, "A sparsity regularization approach to the electromagnetic inverse scattering problem," *IEEE Trans. Antennas Propag.*, vol. 58, no. 1, pp. 145–154, Jan. 2010.
- [6] P. M. van den Berg and R. E. Kleinman, "A contrast source inversion method," *Inverse Problems*, vol. 13, no. 6, pp. 1607–1620, 1997.
- [7] Z. Wei and X. Chen, "Deep-learning schemes for full-wave nonlinear inverse scattering problems," *IEEE Trans. Geosci. Remote Sens.*, vol. 57, no. 4, pp. 1849–1860, Apr. 2019.
- [8] M. Ostadrahimi *et al.*, "Analysis of incident field modeling and incident/scattered field calibration techniques in microwave tomography," *IEEE Antennas Wireless Propag. Lett.*, vol. 10, pp. 900–903, 2011.
- [9] M. Salucci *et al.*, "2-D TM GPR imaging through a multiscale frequency approach in lp spaces," *IEEE Trans. Geosci. Remote Sens.*, vol. 59, no. 12, pp. 10011–10021, Dec. 2021.
- [10] A. Fedeli, "Microwave tomography with LSTM-based processing of the scattered field," *IEEE Open J. Antennas Propag.*, vol. 2, pp. 213–223, 2021.
- [11] J. W. Zhang, S. B. Ye, H. Liu, L. Yi, and G. Y. Fang, "Filtering out antenna effects from GPR data by an RBF neural network," *IEEE Geosci. Remote Sens. Lett.*, vol. 16, no. 9, pp. 1378–1382, Sep. 2019.
- [12] G. Thimm and E. Fiesler, "High-order and multilayer perceptron initialization," *IEEE Trans. Neural Netw.*, vol. 8, no. 2, pp. 349–359, Mar. 1997.
- [13] A. Abubakar, P. M. van den Berg, and T. M. Habashy, "Application of the multiplicative regularized contrast source inversion method on TM and TE-polarized experimental Fresnel data," *Inverse Probl.*, vol. 21, no. 6, pp. S5–S13, 2005.